J. Appl. Comput. Mech., xx(x) (2026) 1-16
DOI: 10.22055/jacm.2026.48823.5532

ISSN: 2383-4536
jacm.scu.ac.ir

Shahid Chamran University of Ahvaz

Journal of Applied and Computational Mechanics

Research Paper

Numerical Study of Defects and Heat Transfer in Repaired Metallic Plates

Brahim Addou[1], Ben-Richou Abderrahim[1], Balouki Abdessamad[2] Azouz Jaouad[3]

[1] Laboratory of Energy Engineering and Materials (LEEM), Faculty of Science and Technology, Sultan Moulay Slimane University, BP 591, 23000 Beni-Mellal, Morocco
[2] Engineering and Applied Physics Team (ETAP), Higher School of Technology, Sultan Moulay Slimane University, BP 591, 23000 Beni-Mellal, Morocco
[3] Department of Mechanical Engineering, National School of Arts and Crafts, Hassan-II University of Casablanca, 20000 Casablanca, Morocco

Received October 14 2025; Revised March 16 2026; Accepted for publication April 14 2026.
✉ Corresponding author: B. Addou (brahim.addou95@gmail.com)

Abstract. This work presents a numerical investigation of transient heat diffusion in a two-dimensional plate containing internal defects subjected to pulsed thermal excitation. The governing heat diffusion equation is solved using the Finite Volume Method (FVM) and the Lattice Boltzmann Method (LBM), implemented through an in-house Fortran 90 code. The numerical model is validated by a grid convergence study and a detailed comparison between both approaches, demonstrating excellent agreement with a maximum relative error below 2.65%. A parametric analysis is conducted to evaluate the influence of defect geometry, including size, depth, and position, on the surface temperature distribution. The results show that increasing defect size leads to higher thermal contrast and more pronounced temperature peaks, whereas defects located deeper or farther from the heated surface exhibit weaker thermal signatures due to enhanced thermal diffusion. The symmetry and localization of the thermal profiles are identified as reliable indicators for defect characterization. The findings confirm the accuracy and efficiency of the Lattice Boltzmann Method for thermal analysis of heterogeneous structures and highlight its potential for applications in thermal-based non-destructive evaluation using infrared thermography.

Keywords: Internal defect; Thermal diffusion; Numerical simulation; Defect parameters; Thermal contrast.

1. Introduction

Defects such as cracks, inclusions, and corrosion can seriously reduce the reliability and service life of engineering materials and structures. These flaws not only weaken mechanical strength but can also influence how a component responds to temperature changes, gradually leading to damage and, in some cases, sudden failure. In industrial pipeline systems, corrosion caused by the transport of aggressive media remains one of the main sources of material degradation, leakage, and environmental risk [1-3]. Similar concerns are found in civil infrastructure, reinforced concrete structures, aerospace components, and mechanical systems, where hidden or subsurface defects can compromise durability and long-term performance [4, 5] For this reason, detecting and evaluating internal defects at an early stage using non-destructive testing (NDT) techniques is essential to maintain structural integrity and support effective predictive maintenance strategies [6-8].

Among the available NDT techniques, infrared thermography has gained widespread acceptance due to its non-contact nature, rapid inspection capability, and sensitivity to subsurface anomalies [9-12]. The method relies on monitoring the surface temperature response of a material subjected to thermal excitation. In homogeneous media, heat transfer follows Fourier's law; however, internal heterogeneities locally disturb heat diffusion, producing measurable temperature contrasts at the surface [13, 14]. This physical principle underpins numerous applications, including the detection of voids in metallic components, delamination in composite materials, and corrosion in industrial and building structures [13, 16]. Experimental and numerical studies have demonstrated that the detectability of defects strongly depends on their geometry, depth, and thermal properties, as well as on the characteristics of the thermal excitation [17, 18].

Accurate interpretation of thermographic data requires reliable numerical modeling, as analytical solutions are generally restricted to idealized geometries and simplified boundary conditions. Numerical techniques, in particular the Finite Volume Method, the Finite Difference Method, and the Finite Element Method have become crucial tools for realistic simulations of heat transfer in defective materials, even though analytical modeling of such phenomena is limited to simple geometries [19-21]. Over the past decade, the LBM has gained increasing attention as a reliable numerical approach for modeling heat transfer processes. Its effectiveness is particularly evident in transient thermal analyses and in the treatment of geometrically complex domains, where conventional methods may encounter limitations. Owing to its mesoscopic formulation, numerical stability, and algorithmic simplicity, LBM has been successfully applied to conduction and convection heat transfer problems [22, 23], with several studies highlighting its favorable stability properties compared to conventional schemes.

Published online: April 18 2026

Table 1. Thermal properties of the studied materials (at 293.15K).

Materials	Thermal Conductivity λ (W/m.K)	Density ρ (Kg/m^3)	Specific Heat Capacity C_p (J/Kg. K)
Steel	44.50	7850	475
Rust	0.60	5242	648.70

Despite these advances, a significant portion of the existing literature remains focused on steady-state conditions or simplified defect configurations, offering limited insight into transient thermal responses under pulsed excitation [24, 25]. Furthermore, systematic comparative studies between FVM and LBM for defect detection applications are still scarce. This lack of comprehensive parametric investigations restricts a detailed understanding of how defect size, depth, and position influence thermal contrast and detection capability [26, 27].

In this context, the present study investigates transient heat transfer in a two-dimensional plate containing internal defects subjected to pulsed thermal loading. A dedicated Fortran 90 code is developed to implement both the FVM and the LBM, allowing consistent numerical comparisons. A detailed parametric analysis is performed to evaluate the influence of defect geometry and thermal properties on surface temperature distributions, with the aim of identifying conditions that enhance thermal contrast and improve defect detectability in thermography-based non-destructive evaluation.

2. Materials and Methods

The geometrical layout of the physical model under consideration is presented in Fig. 1. It consists of a two-dimensional rectangular plate with an internal defect of height l and length L. The vertical walls on the right and left sides of the plate are thermally insulated, while the upper horizontal side is maintained at a constant temperature T_h (heated side), and the lower horizontal side is kept at a constant temperature T_c (cooled side).

The present study aims to develop a numerical model and to investigate heat conduction in a two-dimensional rectangular plate containing an internal defect. The thermophysical properties adopted for the numerical simulations are summarized in Table 1. In this study, diffusive heat transfer is examined through the application of two different numerical approaches. For a two-dimensional computational domain, the time-dependent behavior of the temperature field is governed by the transient heat conduction equation, which can be written in the following form [28]:

$$\rho C_p \frac{\partial T}{\partial t} = \lambda \left\{ \frac{\partial^2 T}{\partial^2 x} + \frac{\partial^2 T}{\partial^2 y} \right\} \tag{1}$$

where,

λ: thermal conductivity of the material, expressed in (W m^{-1} k^{-1})

C_p: represents the specific heat capacity (J K^{-1} Kg^{-1})

ρ: is the material density (Kg m^{-3})

T: represents the temperature at each point and moment

The heat transfer equations to be solved for domains 1 and 2 are as follows:

$$C_P \rho \frac{\partial T}{\partial t} = \lambda \left[\frac{d^2 T}{dx^2} + \frac{d^2 T}{dy^2}\right] \rightarrow \begin{cases} C_{P_1}\rho_1 \dfrac{\partial T_1}{\partial t} = \lambda_1 \left[\dfrac{d^2 T_1}{dx^2} + \dfrac{d^2 T_1}{dy^2}\right] \\ C_{P_2}\rho_2 \dfrac{\partial T_2}{\partial t} = \lambda_2 \left[\dfrac{d^2 T_2}{dx^2} + \dfrac{d^2 T_2}{dy^2}\right] \end{cases} \tag{2}$$

2.1. Boundary conditions

Boundary conditions (BC) can take various forms. They represent the transfers between different parts of the body and its surrounding environment. The continuity constraints at the interface between solid1/solid2 impose:

$$\lambda_{s1} \frac{\partial T}{\partial n} = \lambda_{s2} \frac{\partial T}{\partial n} \tag{3}$$

- Solid/solid interface conditions:

Second-type boundary conditions correspond to the case of heat transfer by conduction across the interface of two solid bodies, 1 and 2, with different thermal conductivities, assuming perfect contact. The surfaces in contact have the same temperature:

$$|x| = \frac{b}{2} \qquad \text{and} \qquad y < a \qquad -\lambda_1 \frac{\partial T_1}{\partial x} = -\lambda_2 \frac{\partial T_2}{\partial x} \tag{4}$$

$$|x| \le \frac{b}{2} \qquad \text{and} \qquad y = a \qquad -\lambda_1 \frac{\partial T_1}{\partial y} = -\lambda_2 \frac{\partial T_2}{\partial y} \tag{5}$$

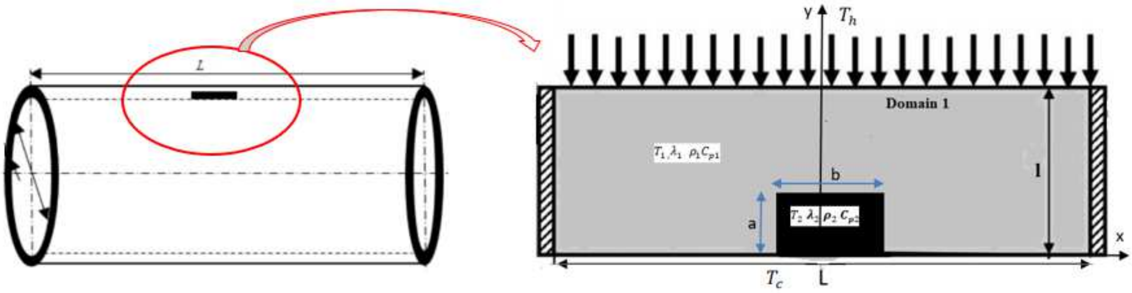

Fig. 1. Geometry of problem.

- Conditions on the lateral surfaces:

$$|x| = \frac{L}{2} \qquad -\lambda_1 \frac{\partial T_1}{\partial x} = 0 \qquad \forall\ 0 \le y \le 1 \tag{6}$$

The use of non-dimensional variables in the equations allows for a better representation of the physical phenomena because they are independent of the measurement unit system used to study them. It can also be said that these variables provide general information, which plays a significant role in similarity analysis. To bring the previous equations into a non-dimensional form, it is necessary to define following variable transformations:

$$\begin{gathered} X = \tfrac{x}{l} \quad ,Y = \tfrac{y}{l} \quad \theta = \tfrac{T-T_C}{T_h-T_C} \qquad 0 \le Y \le 1 \qquad -\tfrac{L}{2} \le X \le \tfrac{L}{2} \\ \varepsilon_y = \tfrac{a}{l} \quad ,\varepsilon_x = \tfrac{b}{l} \quad , \quad e = \tfrac{d}{l} \quad \tau_1 = \tfrac{t}{\tau_{c1}} \ ,\tau_2 = \tfrac{t}{\tau_{c2}} \quad , \tau_{c1} = \tfrac{\rho_2 C_{p2} * l^2}{\lambda_2} = \tfrac{l^2}{\alpha_2} \ ,\tau_{c2} = \tfrac{\rho_1 C_{p1} * l^2}{\lambda_1} = \tfrac{l^2}{\alpha_1} \\ \frac{\partial \theta_1}{\partial \tau_1} = \left\{ \frac{\partial^2 \theta_1}{\partial X^2} + \frac{\partial^2 \theta_1}{\partial Y^2} \right\} \qquad \frac{\partial \theta_2}{\partial \tau_2} = \left\{ \frac{\partial^2 \theta_2}{\partial X^2} + \frac{\partial^2 \theta_2}{\partial Y^2} \right\} \end{gathered} \tag{7}$$

$$|X| = \frac{L}{2} \quad \text{and} \qquad 0 \le Y \le 1 \qquad \frac{\partial^2 \theta_1}{\partial^2 X} = 0 \tag{8}$$

$$|X| = \frac{b}{2} \quad \text{and} \quad Y < a \qquad -\lambda_1 \frac{\partial^2 \theta_1}{\partial^2 X} = -\lambda_2 \frac{\partial^2 \theta_2}{\partial^2 X} \tag{9}$$

$$|X| \le \frac{b}{2} \quad \text{and} \quad Y = a \qquad -\lambda_1 \frac{\partial^2 \theta_1}{\partial^2 Y} = -\lambda_2 \frac{\partial^2 \theta_2}{\partial^2 Y} \tag{10}$$

In numerical methods for solving differential equations, computational areas are converted into small elements, which are shown in Fig. 2. Temperature points are also shown as colored circles.

One of the difficult parts of this problem is the part of applying interface boundary conditions between two materials in contact. Since the interface boundary condition exists only in the elements that are located in the boundary between two materials, therefore a special boundary condition is established in these elements. To solve this problem, it is assumed that all computing elements have different characteristics (C_P, ρ, λ). In this case, due to the different characteristics of each element, the interface boundary condition will be established between all the calculation elements, which is shown in Fig. 3. Now a general equation can be expressed for all elements. In the following, the algebraization of Eq. (2) will be discussed. Figure 3 presents a typical computational element interacting with four adjacent elements.

By two-dimensional integration from Eq. (2), we can write:

$$C_P \rho \frac{T^{n+1} - T^n}{\Delta t} \Delta x \Delta y = \left[\int_y^{y+\Delta y} \left[\left\{ \lambda \frac{dT}{dx} \right\}_e - \left\{ \lambda \frac{dT}{dx} \right\}_w \right] dy + \int_x^{x+\Delta x} \left[\left\{ \lambda \frac{dT}{dy} \right\}_n - \left\{ \lambda \frac{dT}{dy} \right\}_s \right] dx \right] \tag{11}$$

$$C_P \rho \frac{T^{n+1} - T^n}{\Delta t} \Delta x \Delta y = \left[\left[\left\{ \lambda \frac{dT}{dx} \right\}_e - \left\{ \lambda \frac{dT}{dx} \right\}_w \right] \Delta y + \left[\left\{ \lambda \frac{dT}{dy} \right\}_n - \left\{ \lambda \frac{dT}{dy} \right\}_s \right] \right] \Delta x \tag{12}$$

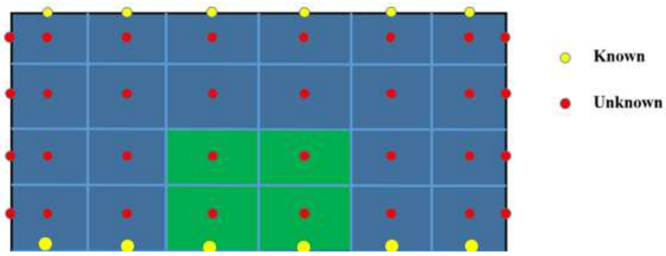

Fig. 2. Meshing known and unknown points.

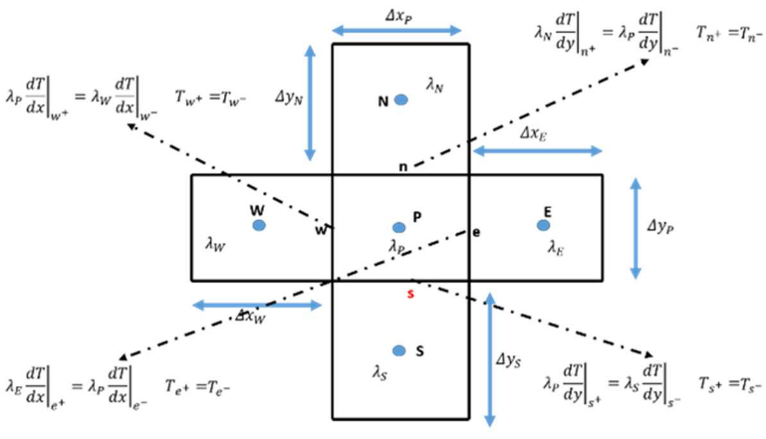

Fig. 3. An example of an element.

Now considering:

$$T_{w^+} = T_{w^-} = T_w \qquad T_{n^+} = T_{n^-} = T_n$$
$$T_{s^+} = T_{s^-} = T_s \qquad T_{e^+} = T_{e^-} = T_e$$

And by using Taylor's expansion and backward scheme, Eq. (12), can be written as follows:

$$C_P\rho\frac{T^{n+1}-T^n}{\Delta t}\Delta x\Delta y = \left[\left[\left\{\lambda\frac{dT}{dx}\right\}_e - \left\{\lambda\frac{dT}{dx}\right\}_w\right]\Delta y + \left[\left\{\lambda\frac{dT}{dy}\right\}_n - \left\{\lambda\frac{dT}{dy}\right\}_s\right]\Delta x\right] \tag{13}$$

$$C_P\rho\frac{T^{n+1}-T^n}{\Delta t}\Delta x_P\Delta y_P = \lambda\left[\left[\left\{\frac{T_e\text{-}T_P}{\frac{1}{2}\Delta x_P}\right\}_e \text{-} \left\{\frac{T_P\text{-}T_w}{\frac{1}{2}\Delta x_P}\right\}_w\right]\Delta y_P + \left[\left\{\frac{T_n\text{-}T_P}{\frac{1}{2}\Delta y_P}\right\}_n \text{-} \left\{\frac{T_P\text{-}T_s}{\frac{1}{2}\Delta y_P}\right\}_s\right]\Delta x_P\right] \tag{14}$$

In Eq. (14), the values of T_n, T_s, T_w, T_e are the temperature values on the boundary of the element P. Since there is no calculation point on the contact surface between the elements, so the temperature of these points must be obtained by other points. For this, the contact boundary condition can be used:

$$\lambda_P\left.\frac{dT}{dx}\right|_{w^+} = \lambda_W\left.\frac{dT}{dx}\right|_{w^-} \qquad \lambda_P\frac{T_P - T_{w^+}}{\frac{1}{2}\Delta x_P} = \lambda_W\frac{T_{w^-} - T_W}{\frac{1}{2}\Delta x_W} \tag{15}$$

$$T_w = \frac{\frac{\lambda_P}{\Delta x_P}T_P + \frac{\lambda_W}{\Delta x_W}T_W}{\frac{\lambda_P}{\Delta x_P} + \frac{\lambda_W}{\Delta x_W}} \qquad T_e = \frac{\frac{\lambda_P}{\Delta x_P}T_P + \frac{\lambda_E}{\Delta x_E}T_E}{\frac{\lambda_P}{\Delta x_P} + \frac{\lambda_E}{\Delta x_E}} \qquad T_s = \frac{\frac{\lambda_P}{\Delta y_P}T_P + \frac{\lambda_S}{\Delta y_S}T_S}{\frac{\lambda_P}{\Delta y_P} + \frac{\lambda_S}{\Delta y_S}} \qquad T_n = \frac{\frac{\lambda_P}{\Delta y_P}T_P + \frac{\lambda_N}{\Delta y_N}T_N}{\frac{\lambda_P}{\Delta y_P} + \frac{\lambda_N}{\Delta y_N}} \tag{16}$$

By inserting Eq. (15) and Eq. (16) in Eq. (14) the following general equation can be reached:

$$C_P\rho\frac{T^{n+1}\text{-}T^n}{\Delta t} = \lambda\left[\left[\left\{\frac{T_e\text{-}T_P}{\frac{1}{2}\Delta x_P^2}\right\}_e \text{-} \left\{\frac{T_P\text{-}T_w}{\frac{1}{2}\Delta x_P^2}\right\}_w\right] + \left[\left\{\frac{T_n\text{-}T_P}{\frac{1}{2}\Delta y_P^2}\right\}_n \text{-} \left\{\frac{T_P\text{-}T_s}{\frac{1}{2}\Delta y_P^2}\right\}_s\right]\right] \tag{17}$$

$$C_{P_P}\rho_P\frac{T_P^{n+1} - T_P^n}{\Delta t} = aeT_E + awT_W + apT_P + asT_S + anT_N \tag{18}$$

and,

$$ae = \frac{2\lambda_P}{\Delta x_P^2}\frac{\frac{\lambda_E}{\Delta x_E}}{\frac{\lambda_P}{\Delta x_P} + \frac{\lambda_E}{\Delta x_E}} \quad , \quad aw = \frac{2\lambda_P}{\Delta x_P^2}\frac{\frac{\lambda_W}{\Delta x_W}}{\frac{\lambda_P}{\Delta x_P} + \frac{\lambda_W}{\Delta x_W}} \quad , \quad as = \frac{2\lambda_P}{\Delta y_P^2}\frac{\frac{\lambda_S}{\Delta y_S}}{\frac{\lambda_P}{\Delta y_P} + \frac{\lambda_S}{\Delta y_S}} \quad , \quad an = \frac{2\lambda_P}{\Delta y_P^2}\frac{\frac{\lambda_N}{\Delta y_N}}{\frac{\lambda_P}{\Delta y_P} + \frac{\lambda_N}{\Delta y_N}}$$

$$ap = -\left[\frac{2\lambda_P}{\Delta y_P^2} + \frac{2\lambda_P}{\Delta x_P^2}\right] + \frac{\lambda_P}{\Delta y_P}\left(\frac{as}{\frac{\lambda_S}{\Delta y_S}} + \frac{an}{\frac{\lambda_N}{\Delta y_N}}\right) + \frac{\lambda_P}{\Delta x_P}\left(\frac{aw}{\frac{\lambda_W}{\Delta x_W}} + \frac{ae}{\frac{\lambda_E}{\Delta x_E}}\right)$$

In general, the equation governing the elements can be expressed as follows:

$$apt[T_P^{n+1} - T_P^n] = aeT_E + awT_W + apT_P + asT_S + anT_N \tag{19}$$

2.2. Alternating Direction Implicit (ADI) method

The ADI scheme is a finite difference approach commonly employed for the numerical solution of elliptic and parabolic partial differential equations. It is particularly well suited for modeling multi-dimensional heat conduction and diffusion problems [21]. The method relies on a directional splitting strategy in which the governing equation is treated implicitly along one spatial direction and explicitly along the other. In the present formulation, the time derivative is approximated using a forward difference scheme, while the spatial derivatives are discretized using central differences. This procedure leads to a set of intermediate algebraic equations that are solved sequentially, advancing the solution from the time level *n* to an intermediate state *n* + 1/2, and subsequently to the next time level *n* + 1. The overall solution process is illustrated schematically on the computational grid in Fig. 4.

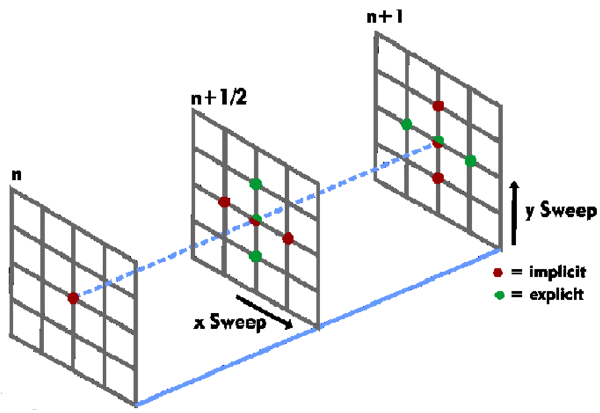

Fig. 4. The grid system for the ADI method depicted.

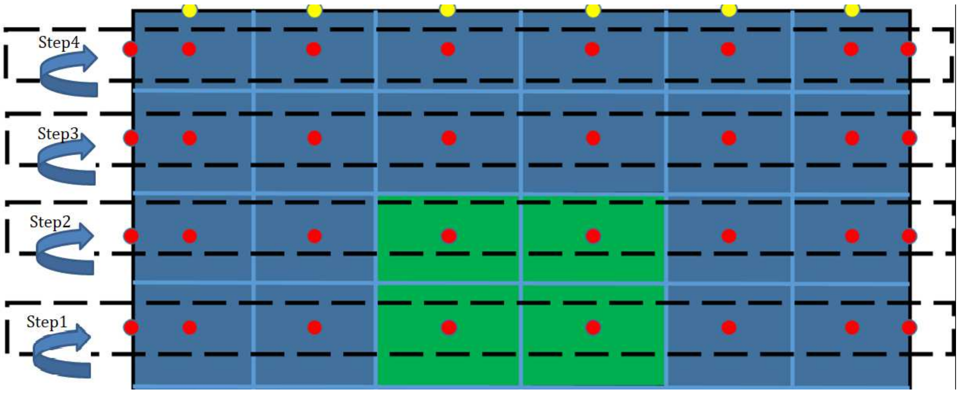

Fig. 5. ADI along *x* axis.

As we know, there are three general methods for solving unstable equations:
- Explicit
- Implicit
- Semi explicit and implicit

In this project, the goal is to solve equations in ADI form. The ADI method is a semi-implicit and semi-explicit method. In the following, the ADI method is explained. In this method, each time step is divided into two sub-steps, i.e., $\mathrm{dt\_new} = \mathrm{dt}/2$, then the elements in a row, as shown in Fig. 5, are all assumed to be unknown. This is done for all *j* = 2, ..., n_y - 1 rows. In the same way, it is repeated in the vertical direction.

ADI along *x* direction:

$$C_{P_P}\rho_P \frac{T_P^{n+1} - T_P^n}{\frac{\Delta t}{2}} = aeT_E + awT_W + apT_P + asT_S + anT_N \tag{20}$$

$$-aeT_E^{n+\frac{1}{2}} - awT_W^{n+\frac{1}{2}} + [2apt - ap]T_P^{n+\frac{1}{2}} = +asT_S^n + anT_N^n + 2aptT_P^n \tag{21}$$

ADI along y direction:

$$-asT_S^{n+1} - anT_N^{n+1} + [2apt - ap]T_P^{n+1} = aeT_E^{n+\frac{1}{2}} + awT_W^{n+\frac{1}{2}} + 2aptT_P^{n+\frac{1}{2}} \tag{22}$$

- Sing TDMA for solving equation

The Tridiagonal Matrix Algorithm (TDMA) is a two-step procedure that combines features of both direct and iterative methods. Common iterative methods include Gauss-Seidel and Jacobi, while direct methods include Gaussian elimination and LU decomposition. In TDMA, we first treat all variables along one direction as unknowns and assume that the variables in the other direction are known. In the second step, we reverse these roles, considering the previously known variables as unknowns and vice versa.

- For step 1:

$$-aeT_E^{n+\frac{1}{2}} - awT_W^{n+\frac{1}{2}} + [2apt - ap]T_P^{n+\frac{1}{2}} = +asT_S^n + anT_N^n + 2aptT_P^n \tag{23}$$

First, supply the arrays of a (below diagonal), b (diagonal), c (above diagonal), and d (right side vector).

$b_{i,j} = 2\ a_{pt} - a_p$ (coefficient at the point P)

$a_{i,j} = -a_e$ (coefficient at the east neighbor)

$c_{i,j} = -a_w$ (coefficient at the west neighbor)

$d_{i,j}$ collects the known terms of the right-hand side, evaluated at the previous time step or at the intermediate half-step.

3. Thermal Lattice Boltzmann Method

The numerical solution of the Boltzmann equation requires discretization in both time and space. In the Lattice Boltzmann framework, the particle velocity vector $\vec{e_k}$ is defined over a finite set of discrete directions in space, commonly referred to as predefined lattice velocities [22-24, 29]. Using this method, the temperature distribution function's kinetic equation can be expressed as follows:

$$\frac{\partial g_k(\vec{r},t)}{\partial t} + \vec{e_k}\ \nabla g_k.\ (\vec{r},t) = -\frac{1}{\tau_\theta}[g_k(\vec{r},t) - g_k^{eq}(\vec{r},t)] \tag{24}$$

The dimensionless temperature distribution function is described by the following discrete form of the Boltzmann equation:

$$g_k(x+\Delta x,\ y+\Delta y,\ t+\Delta t) - g_k(x,\ y,\ t) = -\frac{\Delta t}{\tau_\theta}[g_k(x,\ y,\ t) - g_k^{eq}(x,\ y,\ t)] \tag{25}$$

where τ_θ represents the collision relaxation time for energy.

Nonetheless, the focus of this article revolves around addressing two-dimensional diffusion and D2Q9 lattice problems. A specific configuration is employed in this research endeavor. The resolution of Eq. (24) is carried out on a discretized domain, known as the lattice. This discretization involves a finite number of nodes referred to as lattices. The system undergoes a two-step evolution: collision and propagation, the latter also being known as advection.

Equation (25) can therefore be solved in two steps:

- Collision:

$$g_k(x, y, t+\Delta t)-g_k(x, y, t)=-\frac{\Delta t}{\tau_\theta}[g_k(\vec{r},t)-g_k^{eq}(\vec{r},t)] \tag{26}$$

- Propagation or streaming:

$$g_k(x+\Delta x, y+\Delta y, t+\Delta t)=g_k(x, y, t+\Delta t) \tag{27}$$

For the D2Q9 lattice, nine discrete velocity vectors $\vec{e_k}$ and their corresponding weighting factors ω_k are employed to ensure second-order accuracy and isotropy of the thermal field:

$$\omega_k=\begin{cases}\frac{4}{9} & k=0\\ \frac{1}{9} & k=1\text{-}4\\ \frac{1}{36} & k=5\text{-}8\end{cases} \tag{28}$$

$$e_k=\begin{cases}(0,0) & k=0\\ \left(\cos\frac{\pi(k-1)}{2},\sin\frac{\pi(k-1)}{2}\right)\frac{\Delta x}{\Delta t}, & k=1\text{-}4\\ \sqrt{2}\left(\cos\frac{\pi(2k-1)}{4},\sin\frac{\pi(2k-1)}{4}\right)\frac{\Delta x}{\Delta t}, & k=5\text{-}8\end{cases} \tag{29}$$

In heat transfer modeling, the macroscopic temperature is calculated by taking the summation of the temperature distribution functions across all discrete lattice directions:

$$\varphi(\vec{r},t)=\sum_{k=0}^{b}g_k(\vec{r},t) \tag{30}$$

After the streaming step, certain distribution functions particularly those located at the domain boundaries or adjacent to solid walls are not known. The role of the boundary condition is thus to reconstruct these missing distribution functions. This situation is schematically represented in Fig. 6, which highlights the issue at a boundary node.

3.1. Thermal boundary conditions

Two approaches are possible for applying boundary conditions at the interface between two regions. In the first method, distinct relaxation time coefficients are defined for each zone. As for the second method, in addition to establishing different relaxation time coefficients between the two regions, the associated differential equation is modified into an algebraic form. The temperature is then calculated at the boundary. A temperature $T_{top}=1$ is imposed at the upper wall, and bottom $T_{bottom}=0$ at the lower wall. The implementation of these conditions for the distribution function g is as follows:

- At the top wall:

$$g_{ny,8}=T_{top}*\{w(8)+w(6)\}-g_{ny,6} \tag{31a}$$

$$g_{ny,7}=T_{top}*\{w(7)+w(5)\}-g_{ny,5} \tag{31b}$$

$$g_{ny,4}=T_{top}*\{w(4)+w(2)\}-g_{ny,2} \tag{31c}$$

- At the bottom wall:

$$g_{0,2}=T_{down}*\{w(2)+w(4)\}-g_{0,4} \tag{32a}$$

$$g_{0,5}=T_{down}*\{w(5)+w(7)\}-g_{0,7} \tag{32b}$$

$$g_{0,6}=T_{down}*\{w(6)+w(8)\}-g_{0,8} \tag{32c}$$

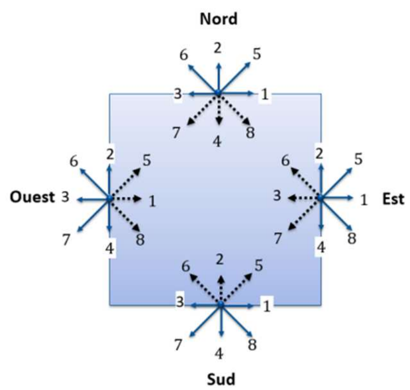

Fig. 6. D2Q9 model.

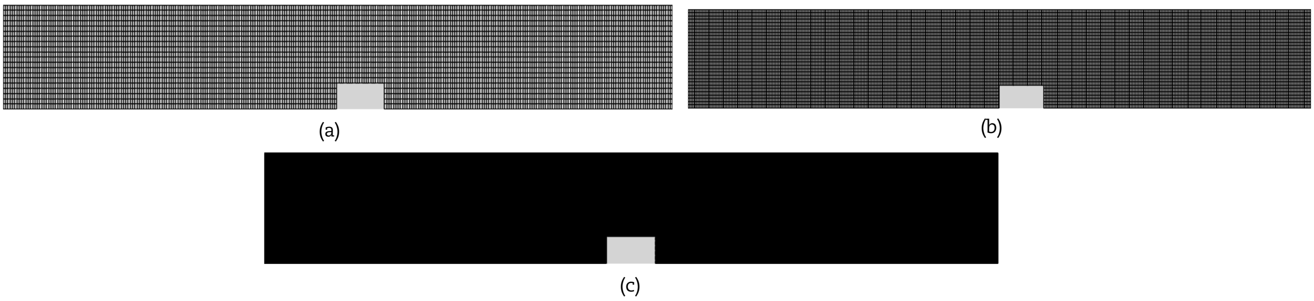

Figs. 7. Mesh structures of a rectangular geometry, (a) Mesh 1, (b) Mesh 2, (c) Mesh 3.

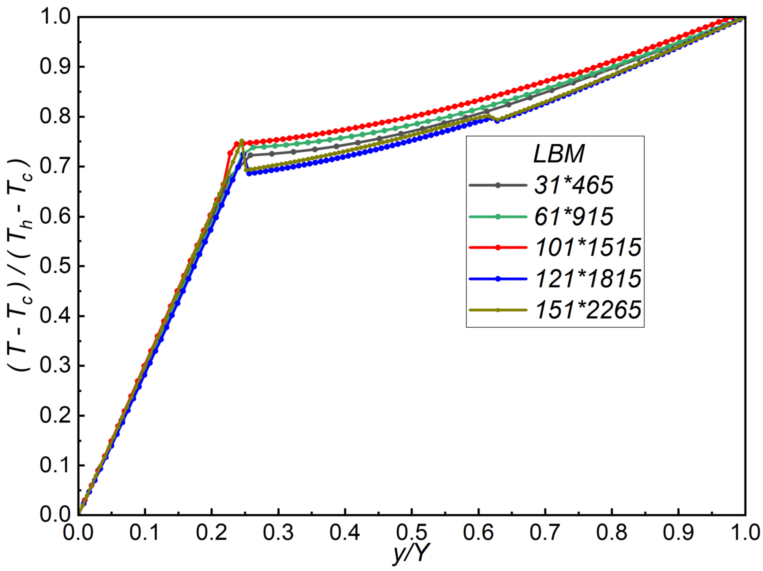

Fig. 8. Effect of grid size on temperature variations at the midpoint x/X = 0.5

For the adiabatic vertical walls, the application of boundary conditions is done using the equations:

$$g_{0,1} = g_{0,3}\ ,\ g_{0,5} = g_{0,7}\ ,\ g_{0,8} = g_{0,6} \tag{33a}$$

$$g_{n,1} = g_{n,3}\ ,\ g_{n,5} = g_{n,7}\ ,\ g_{n,8} = g_{n,6} \tag{33b}$$

where n denotes the grid on the boundary.

4. Results of Numerical Simulation

4.1. Validation of the numerical code

The Fortran 90 code was validated by comparing numerical solutions of the diffusion equation obtained using the lattice-based approach and the finite-volume formulation. A grid sensitivity analysis was performed to examine the effect of mesh resolution on the results. Several mesh sizes were considered, and the temperature profiles were evaluated along the midline of the computational domain. The comparison showed good agreement between the two methods. An appropriate mesh resolution was identified to ensure numerical accuracy while maintaining reasonable computational cost.

4.2. Mesh study

To assess the impact of mesh size on the numerical results, the problem was solved using grids of various resolutions, as illustrated in Figs. 7. The influence of the mesh was evaluated by examining the variations in temperature distribution along the centerline of the geometry, specifically at x/Y = 0.5 for each grid size considered.

The dimensionless vertical temperature distribution at x/X = 0.5 along the height of the plate is presented in Fig. 8. The governing diffusion equation was solved using the lattice Boltzmann method (LBM). To evaluate the influence of grid resolution on the numerical results, a grid independence study was conducted using five different mesh resolutions: 31x465, 61x915, 101x1515, 121x1815, and 151x2565.

The comparison of the temperature profiles shows that the numerical solutions gradually converge as the mesh is refined. In particular, the profiles obtained with the finer grids become almost indistinguishable, indicating that the solution is nearly independent of the grid resolution. It can also be observed that further refinement beyond the 101×1515 mesh leads to only minor changes in the temperature distribution while significantly increasing the computational cost. Therefore, the 101×1515 grid can be considered sufficiently refined to ensure accurate numerical results without unnecessary computational expense.

The results shown in Fig. 9 indicate that the maximum relative error between the two numerical approaches, evaluated using Eq. (34), does not exceed 2.65%. This limited discrepancy reflects a very good agreement between the temperature distributions predicted by the two methods over the entire domain. Such an error level remains well within the range commonly accepted for numerical validation and confirms the consistency of the obtained results.

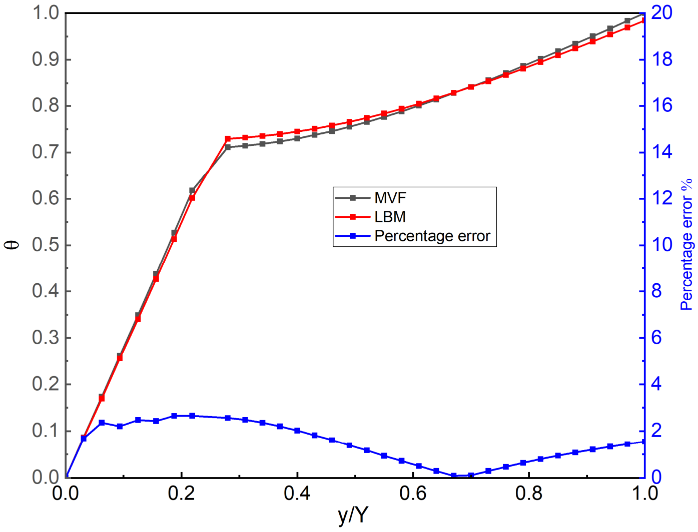

Fig. 9. Validation of numerical simulation.

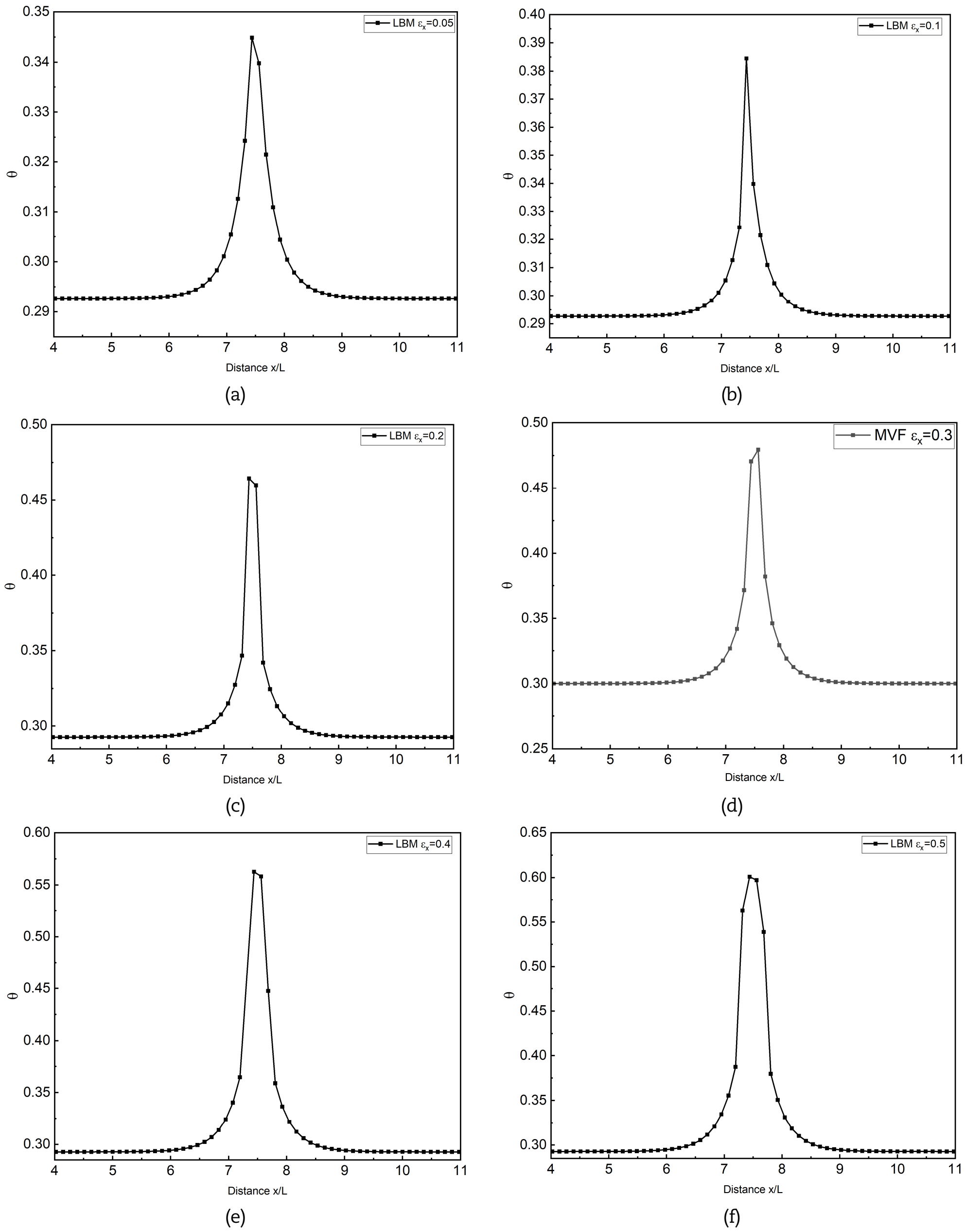

Fig. 10. Comparison of the temperature evolution for different defect sizes for ε_y = 0.3.

Therefore, we can confirm that our code functions correctly, allowing us to proceed with modifications for addressing subsequent problems.

$$\text{Error } (\%) = \frac{(T_{MVF} - T_{LBM})}{T_{MVF}} \times 100 \tag{34}$$

5. Study of the Influence of Defect Parameters

5.1. Influence of the dimensionless size of the defect

Using a variety of defect geometries with different dimensions, a thorough parametric analysis was carried out to examine the effects of defect size, position, and depth on the material's surface temperature distribution. Defects with a constant depth of $\varepsilon_y = 0.3$ were embedded within the inner wall of the material, with defect sizes ranging from $\varepsilon_x = 0.05$ to $\varepsilon_x = 0.5$.

The analysis was performed by calculating the temperature profiles using the Lattice Boltzmann Method (LBM), which effectively models microscopic interactions to predict thermal behavior on a macroscopic scale. Figs. 10(a) to 10(f) illustrate the normalized temperature distribution (x/L) along the surface for various defect sizes (ε_x). Each figure corresponds to a specific defect size within the defined range, illustrating how variations in defect dimensions influence the resulting surface temperature distribution. The temperature profiles reveal significant variations influenced by the defect size, emphasizing its critical role in determining the thermal behavior of the material. These findings highlight the effectiveness of the LBM in analyzing the thermal effects of structural irregularities with high precision, providing valuable insights for materials design and optimization in applications sensitive to thermal distributions.

Across in all graphs of Figs. 10(a) to 10(f), a distinct peak is observed in the distribution temperature, matching the location of the flaw in the material. The peak's sharpness and height reflect the level of thermal contrast produced by the defect. As the defect size increases (from $\varepsilon_x = 0.05$ to $\varepsilon_x = 0.5$), the peak height also increases, suggesting a more pronounced thermal contrast associated with larger defects. For small defects ($\varepsilon_x = 0.05$), the temperature distribution is narrower, indicating that the thermal effect is more localized. In contrast, as the defect size increases, the distribution widens, indicating that the defect influences a larger area of the material. This widening confirms that larger defects exert a greater influence on the global thermal field.

The temperature profiles are symmetrical around the defect location, confirming that heat flow is equally influenced on both sides along the X-axis. This symmetry also suggests a uniform distribution of the defect within the material and the absence of external disturbances. The temperature peaks are critical indicators, as their height and width provide information about the size and severity of the defect. Larger defects cause more pronounced peaks, making them easier to detect. As the defect size increases, the thermal contrast becomes more significant. These results highlight how internal defects affect heat transfer and underscore the importance of such analysis for developing non-destructive testing methods based on thermal signatures.

The MVF and LBM methods seem to provide similar results across most of the domain, suggesting good agreement in general (see Fig. 11). However, the spike in percentage error at the peak indicates that there are regions where these two methods differ significantly, possibly due to differences in how they handle sharp gradients or nonlinearities.

The results presented in Fig. 12, illustrate how the temperature difference varies with defect size, considering a range of defect depths (ε_y) spanning from 0 to 1. For each defect depth, a distinct minimum in the temperature difference is observed. When the defect is located near the heated surface, the minimum is well-defined and sharply localized, allowing for a more accurate determination of defect depth. In contrast, as the defect moves further away from the surface where the heat flux is applied, the corresponding minimum becomes less distinct, leading to a decrease in the precision of defect localization.

The graphs in Figs. 13(a) to 13(d) illustrate the variation of the maximum average temperature difference $\Delta\theta_{\text{moy}}$ as a function of the relative defect size for various defect depths ε_y. Each graph compares the results obtained from two numerical methods (LBM and FVM) and also includes the percentage error between these two approaches.

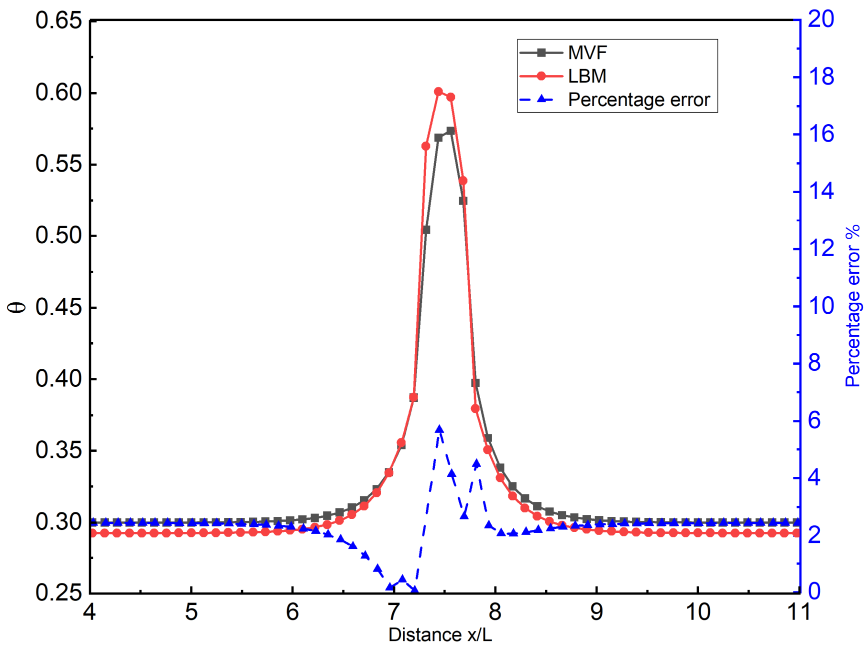

Fig. 11. Comparison of the maximum relative error between the two methods.

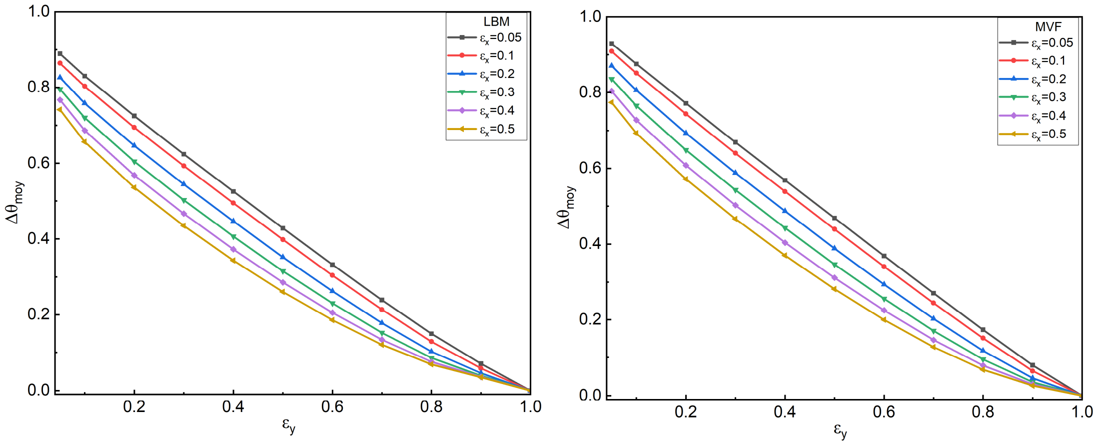

Fig. 12. Influence of the defect size on the average temperature difference $\Delta\theta_{moy}$.

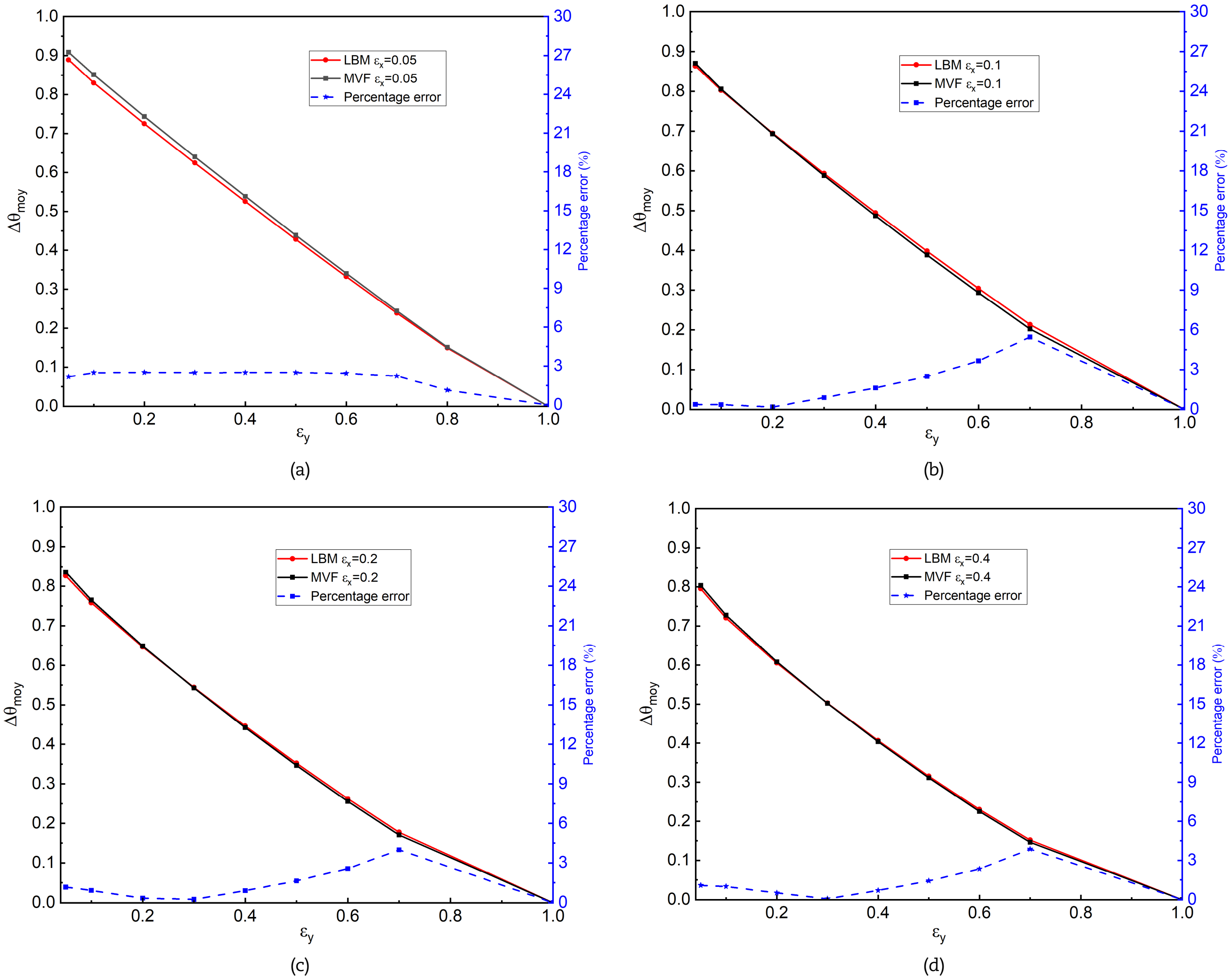

Fig. 13. Influence of the defect size on the average temperature difference $\Delta\theta_{moy}$ with the relative error, (a) $\varepsilon_x = 0.05$, (b) $\varepsilon_x = 0.1$, (c) $\varepsilon_x = 0.2$, (d) $\varepsilon_x = 0.4$.

As the relative size (ε_y) of the defect increases (i.e., as the upper part of the defect moves away from the lower edge of the plate), the maximum thermal contrast $\Delta\theta_{moy}$ decreases steadily, which is consistent across all the graphs presented. This decrease in $\Delta\theta_{moy}$ indicates that defects located farther from the heated edge are more difficult to detect due to the reduced thermal contrast. Moreover, as the depth of the defect ε_y increases, $\Delta\theta_{moy}$ decreases even more rapidly with e, suggesting that deeper defects exhibit even lower thermal contrasts, making their detection even more complex.

Figures 14 illustrates the temperature profiles computed for various defect sizes (ε_x = 0.05 to 0.5), showing that each defect depth exhibits a specific position associated with a minimum in the average temperature difference ($\Delta\theta_{moy}$), This behavior indicates a threshold of detectability linked to the geometric characteristics of the defect. The comparison between LBM and FVM results reveals a generally low percentage error, confirming good agreement between the two numerical methods. However, this error tends to increase with defect depth, suggesting a decline in detection accuracy for deeper defects.

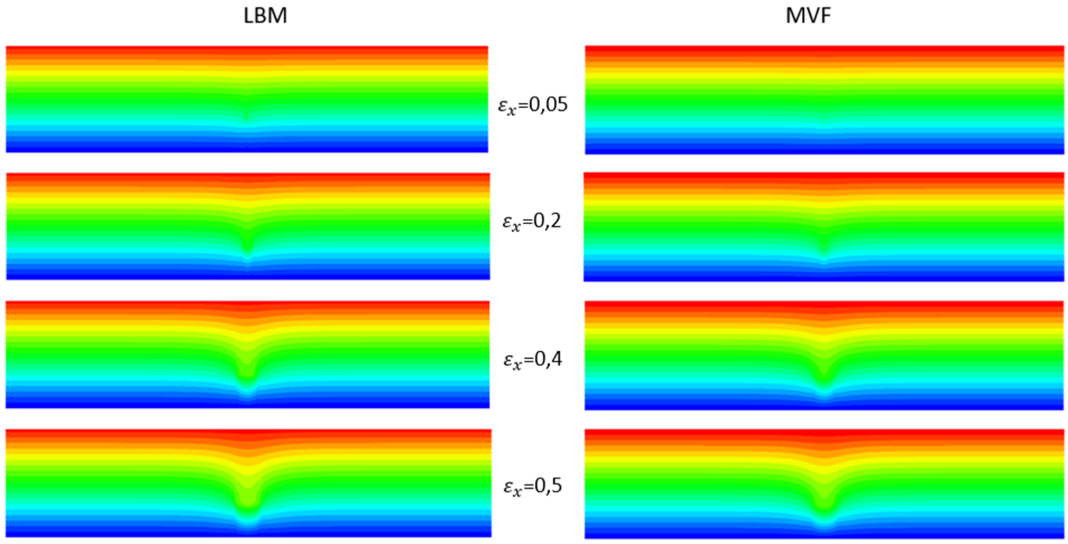

Fig. 14. Temperature contours with different defect sizes.

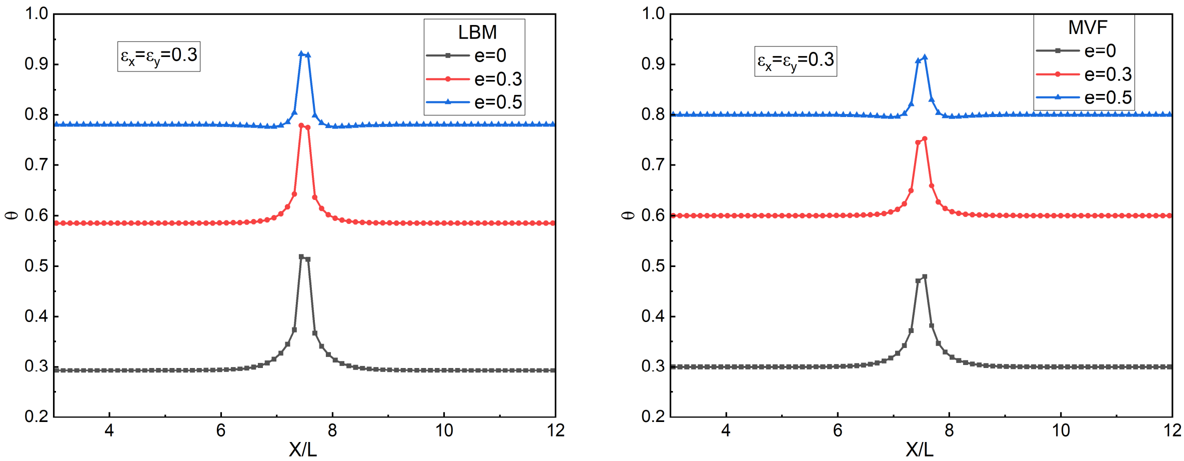

Fig. 15. Impact of different defect positions on the temperature profile θ for $\varepsilon_y = \varepsilon_x = 0.3$.

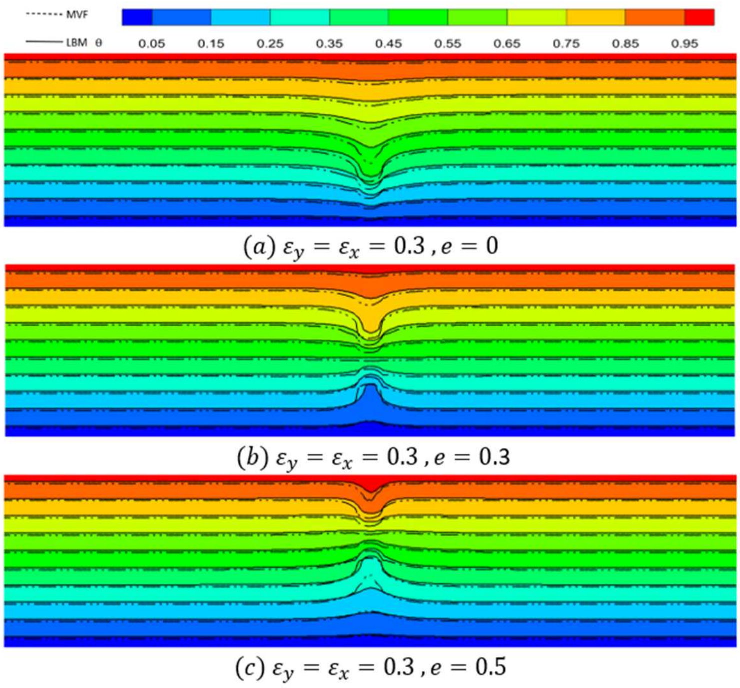

Fig. 16. Temperature contours with different defect positions for $\varepsilon_y = \varepsilon_x = 0.3$.

5.2. Effect of the position

We maintain the same structure used and consider three defects of the same nature, size, and depth. Their positions relative to the lower face vary (see Fig. 15). The defects are located at distances from the lower face of e = 0, e = 0.3 and e = 0.5. The temperature evolution along this axis suggests that defects located closer to the heated surface correspond to higher temperature values, as opposed to the behavior observed in the average temperature difference $\Delta\theta_{moy}$, thereby enhancing the detection of anomalies. This observation considers the relatively small dimensions of the defect compared to the overall structure. Furthermore, the analysis of surface temperature variation along the vertical axis traversing the defect zone clearly reveals the presence of these anomalies within the material.

The temperature contour plots shown in subfigures (a), (b), (c) illustrate the effect of defect position on the thermal field within the structure. The solid and dashed curves represent the results obtained from the two numerical approaches considered, allowing a direct comparison of their predictions. A very close overlap between the contours is observed, indicating a strong consistency between the computed temperature fields. When the defect is located near the heated surface, the thermal disturbance is more pronounced, leading to a noticeable deformation of the isotherms. As the defect moves farther away from the surface, this perturbation gradually weakens, reflecting a reduction in thermal contrast. These observations are in full agreement with the trends discussed previously and highlight the significant role played by defect position in shaping the overall thermal response of the structure.

6. Effect of Depth

According to Fig .17, which represents the evolution of temperature at different defect depths, we observe that the amplitude of the peak reflecting the presence of the defect is greater, which is consistent with the results from both methods. These findings indicate that deeper defects lead to increased thermal contrast, thereby facilitating their detection.

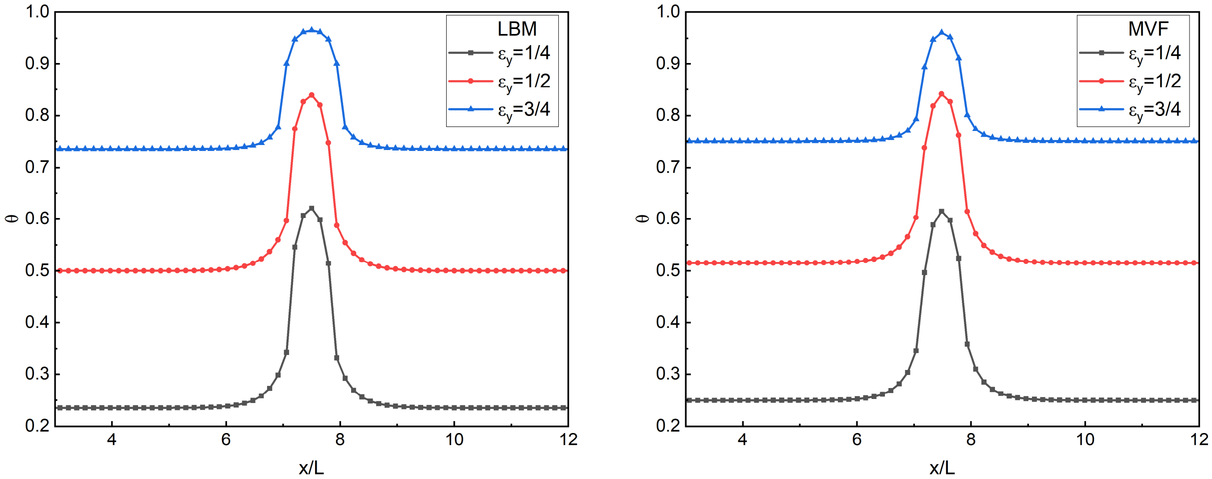

Fig. 17. Impact of defect depth on the temperature profile θ for $\varepsilon_x = 3/4$ and $e = 0$.

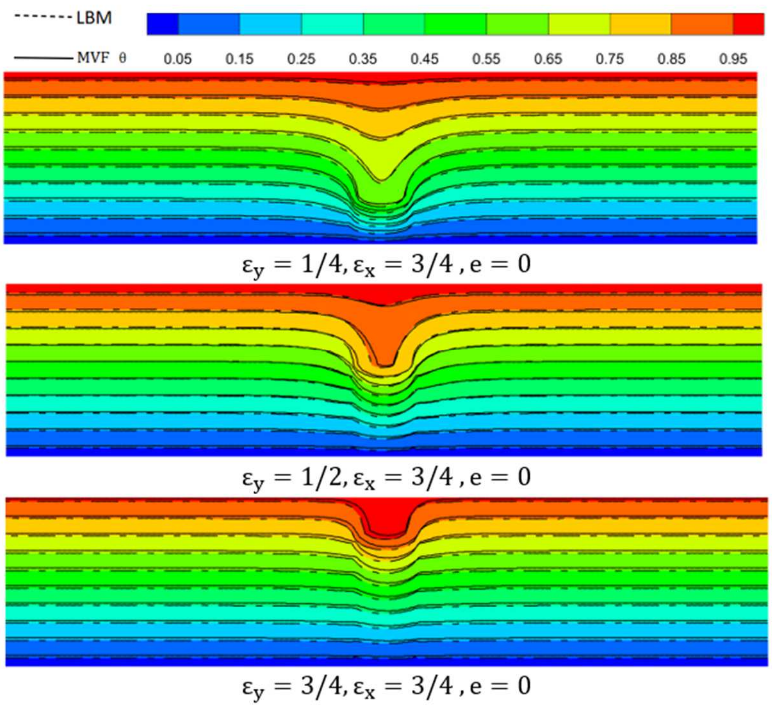

Fig. 18. Temperature contours with different defects effect of depth.

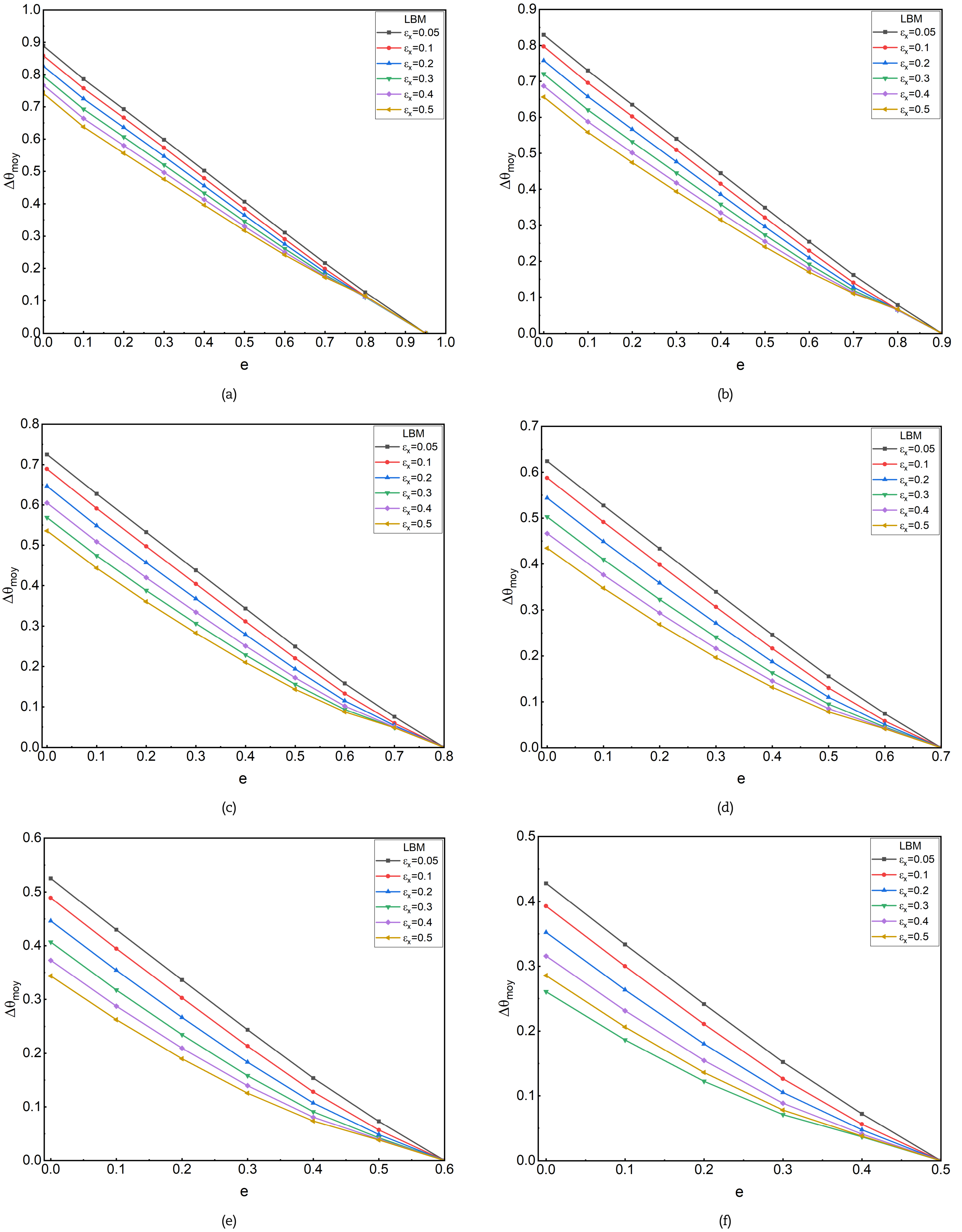

Fig. 19. Influence of defect size and depth on temperature difference $\Delta\theta_{moy}$, (a) $\varepsilon_y = 0.05$, (b) $\varepsilon_y = 0.1$, (c) $\varepsilon_y = 0.2$, (d) $\varepsilon_y = 0.3$, (e) $\varepsilon_y = 0.4$, (f) $\varepsilon_y = 0.5$.

The results from Figs. 18 and 19 show that the maximum thermal contrast $\Delta\theta_{moy}$ decreases as the relative position e of the defect moves away from the lower edge of the plate, making defects located further away more difficult to detect. Additionally, for larger defects ε_x, the thermal contrast is also reduced, as these defects dissipate heat more efficiently. Finally, an increase in defect depth ε_x leads to an overall decrease in thermal contrast, confirming that deeper defects are harder to detect due to greater thermal diffusion through the surrounding material.

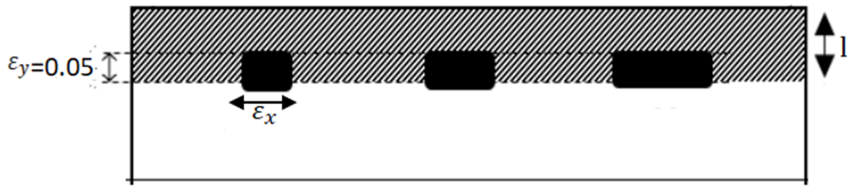

Fig. 20. The plate with the three rust sizes.

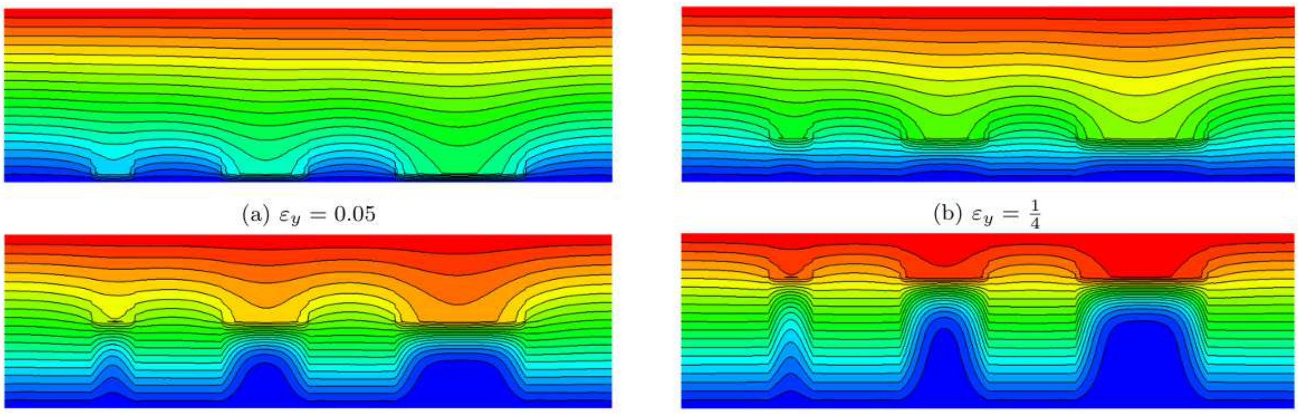

(a) $\varepsilon_y = 0.05$

(b) $\varepsilon_y = \frac{1}{4}$

(c) $\varepsilon_y = \frac{1}{2}$

(d) $\varepsilon_y = \frac{3}{4}$

Fig. 21. Thermal contrast corresponding to three defect sizes at various depths.

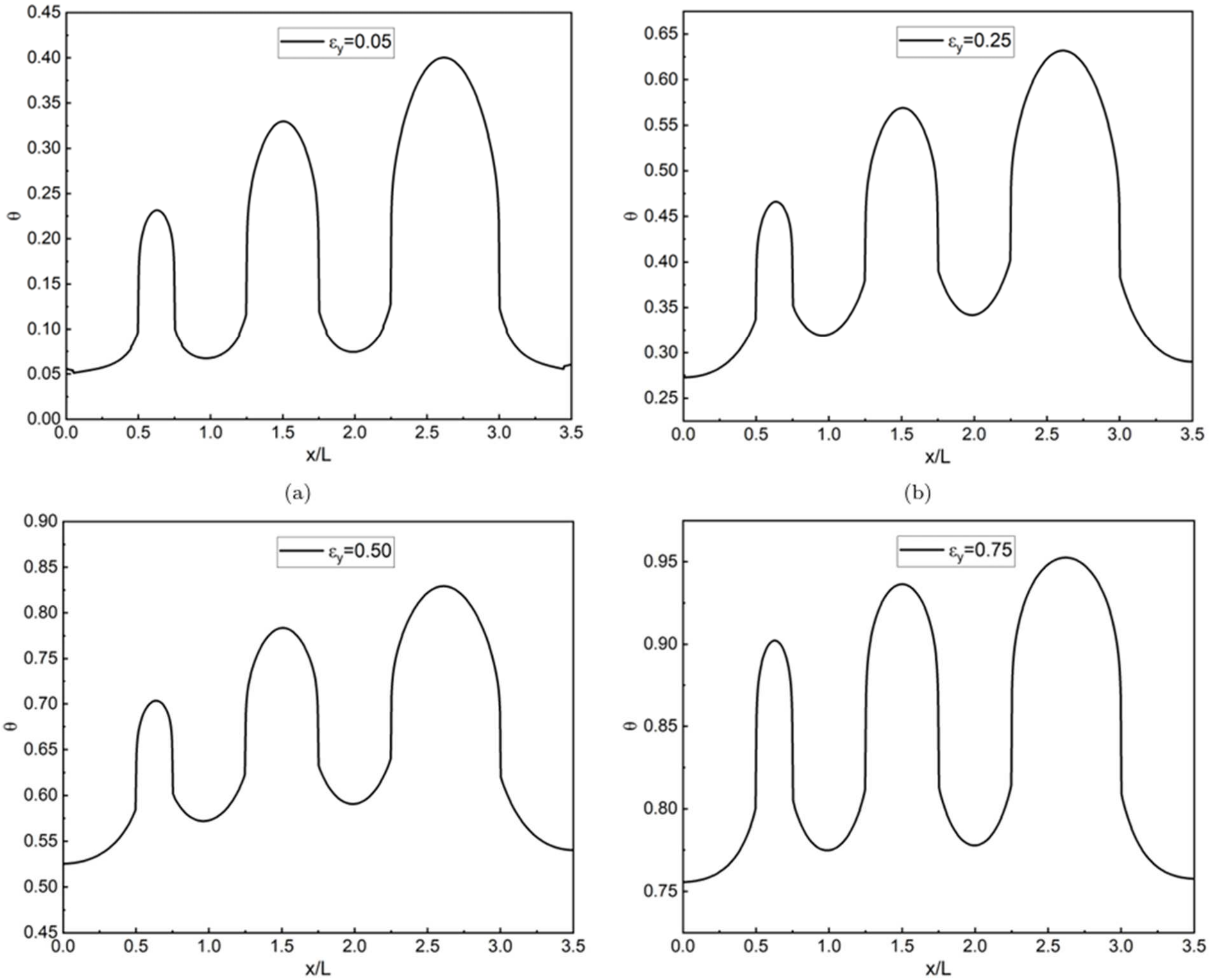

(a)

(b)

(c)

(d)

Fig. 22. (a)–(d) Temperature profile evolution of the rust defect for the four different depths.

7. Influence of Three Defect Sizes

We use the same structure previously studied by incorporating three defects of the same nature to evaluate the influence of their size. These defects, which have varying depths, are illustrated by a two-dimensional rectangular geometry (see Fig. 20) and are located on the inner wall.

The results obtained from the thermal response of the structure, displayed in Figs. 21(a) to 21(d), confirm that defects of different sizes can be identified by analyzing the temperature profile. Notably, the temperature variation along the OX axis exhibits significant differences based on defect size. Higher temperature values are observed in regions corresponding to deeper defects, while a moderate increase is also detected in zones with shallower defects. This results in a pronounced thermal gradient between the defective regions and the surrounding intact material, thereby enhancing the visibility of anomalies through thermal imaging.

Figures 22 (a) to (d) shows the evolution of the dimensionless temperature profile θ along the horizontal direction x/L for different values of the parameter ε_y, which represents the vertical size of the defect ε_y = 0.05, 0.25, 0.50, and 0.75. The temperature varies smoothly along the surface, with localized disturbances appearing above the defective regions. These disturbances are reflected by temperature peaks, indicating a local modification of the heat flux caused by the presence of the defect.

As the value of ε_y increases, the influence of the defect on the thermal field becomes more pronounced. The temperature peaks gradually become higher and the thermal gradients stronger, showing a greater accumulation of heat above the defect. This behavior can be explained by the insulating nature of the defect, which locally reduces heat conduction. As a result, larger defects produce stronger thermal contrasts, making them easier to detect during infrared thermographic inspections, whereas smaller defects generate weaker temperature variations and are therefore more difficult to identify.

8. Conclusion

This work has presented a numerical investigation of heat transfer in a structure containing internal defects, using two complementary computational approaches. The numerical framework was validated through the solution of the heat diffusion equation combined with a mesh convergence analysis, which demonstrated the consistency and accuracy of the simulations. The very close agreement between the results obtained with both approaches confirms the reliability of the numerical predictions and highlights the relevance of the adopted modeling strategy for complex thermal problems. The parametric analysis carried out in this study showed that defect geometry plays a key role in shaping the thermal response of the structure. In particular, defects with larger dimensions and those located near the heated surface were found to generate stronger thermal contrasts, while defects positioned deeper or farther from the heat source led to weaker surface temperature signatures. In addition, the symmetry of the temperature profiles and the evolution of localized thermal peaks were shown to provide meaningful information for defect identification and characterization. Overall, the results underline the effectiveness of the proposed numerical approach for analyzing heat transfer in defective structures. The findings contribute to a better understanding of the thermal behavior induced by internal defects and provide useful guidance for improving thermal-based non-destructive evaluation techniques in industrial applications.

Author Contributions

B. Addou was responsible for conceptualization, methodology, software development, validation, formal analysis, visualization, and preparation of the original draft. B.-R. Abderrahim contributed to the methodology, investigation, and review and editing of the manuscript. B. Abdessamad carried out the investigation, data curation, and project administration. A. Jaouad contributed to resources and funding acquisition. The manuscript was written with contributions from all authors. All authors discussed the results, reviewed, and approved the final version of the manuscript.

Acknowledgments

Not applicable.

Conflict of Interest

The authors declared no potential conflicts of interest concerning the research, authorship, and publication of this article.

Funding

The authors received no financial support for the research, authorship, and publication of this article.

Data Availability Statements

The datasets generated and/or analyzed during the current study are available from the corresponding author on reasonable request.

References

[1] Cheng, C.C., Cheng, T.M., Chiang, C.H., Defect detection of concrete structures using both infrared thermography and elastic waves, *Automation in Construction*, 18, 2008, 87–92.
[2] Ghavamian, A., Mustapha, F., Baharudin, B.T.H.T., Yidris, N., Detection, localisation and assessment of defects in pipes using guided wave techniques: A review, *Sensors*, 18, 2018, 4470.
[3] Zhao, Y., Yu, J., Wu, Y., Jin, W., Critical thickness of rust layer at inner and out surface cracking of concrete cover in reinforced concrete structures, *Corrosion Science*, 59, 2012, 316–323.
[4] Doshvarpassand, S., Wang, X., Sub-surface defect depth approximation in cold infrared thermography, *Sensors*, 22, 2022, 7098.
[5] Bauer, E., Pavón, E., Barreira, E., De Castro, E.K., Analysis of building facade defects using infrared thermography: Laboratory studies, *Journal of Building Engineering*, 6, 2016, 93–104.
[6] Sun, J.G., Analysis of pulsed thermography methods for defect depth prediction, *Journal of Heat Transfer*, 128, 2006, 329–338.
[7] Milovanovic, B., Banjad Pecur, I., Štirmer, N., The methodology for defect quantification in concrete using IR thermography, *Journal of Civil Engineering and Management*, 23, 2017, 573–582.

[8] Nguyen, Q.T., Caré, S., Millard, A., Berthaud, Y., Analyse de la fissuration du béton armé en corrosion accélérée, *Comptes Rendus Mécanique*, 335, 2007, 99–104.
[9] Bates, D., Smith, G., Lu, D., Hewitt, J., Rapid thermal non-destructive testing of aircraft components, *Composites Part B: Engineering*, 31, 2000, 175–185.
[10] Zou, Q., He, X., On pressure and velocity boundary conditions for the lattice Boltzmann BGK model, *Physics of Fluids*, 9, 1997, 1591–1596.
[11] Ranjit, S., Kang, K., Kim, W., Investigation of lock-in infrared thermography for evaluation of subsurface defects size and depth, *International Journal of Precision Engineering and Manufacturing*, 16, 2015, 2255–2264.
[12] Inagaki, T., Ishii, T., Iwamoto, T., On the NDT and E for the diagnosis of defects using infrared thermography, *NDT and E International*, 32, 1999, 247–257.
[13] Liou, T.M., Wei, T.C., Wang, C.S., Investigation of nanofluids on heat transfer enhancement in a louvered microchannel with lattice Boltzmann method, *Journal of Thermal Analysis and Calorimetry*, 135, 2019, 751–762.
[14] Wang, Y., Chung, S.J., Leonard, J.P., Cho, S.K., Phuoc, T., Soong, Y., Chyu, M.K., Cooling performance of nanofluids in a microchannel heat sink, *Proceedings of the ASME Micro/Nanoscale Heat and Mass Transfer International Conference*, 1, 2010, 617–623.
[15] Montinaro, N., Cerniglia, D., Pitarresi, G., Detection and characterisation of disbonds on fibre metal laminate hybrid composites by flying laser spot thermography, *Composites Part B: Engineering*, 108, 2017, 164–173.
[16] Elballouti, A., Belattar, S., Laaidi, N., Thermal nondestructive study of defects of pipe form in the roadway, *Physics and Chemistry News*, 55, 2010, 34–37.
[17] Fox, M., Coley, D., Goodhew, S., De Wilde, P., Time-lapse thermography for building defect detection, *Energy and Buildings*, 92, 2015, 95–106.
[18] Moskovchenko, A.I., Švantner, M., Vavilov, V.P., Chulkov, A.O., Characterizing depth of defects with low size/depth aspect ratio and low thermal reflection by using pulsed IR thermography, *Materials*, 14, 2021, 1886.
[19] Abdellatif, O., Belattar, S., Tmiri, A., El Ballouti, A., Jadida, E., Two-dimensional analysis of thermal non destructive evaluation by the numerical method of control volumes, *IV International workshop- Advances in signal processing for Nondestructive Evaluation of Materials*, X.P.V. Maldague, Vol. 6 Technical Editor, Canada, 2001.
[20] Beskok, A., Karniadakis, G.E., Simulation of heat and momentum transfer in micro-geometries, *Journal of Thermophysics and Heat Transfer*, 8, 1994.
[21] Abimbola, A., Bright, S., Alternating-direction implicit finite-difference method for transient 2D heat transfer in a metal bar using finite difference method, *International Journal of Scientific and Engineering Research*, 6, 2015, 105–108.
[22] Succi, S., Sbragaglia, M., Ubertini, S., Lattice Boltzmann method, *Scholarpedia*, 5, 2010, 9507.
[23] Mishra, S.C., Roy, H.K., Solving transient conduction and radiation heat transfer problems using the lattice Boltzmann method and the finite volume method, *Journal of Computational Physics*, 223, 2007, 89–107.
[24] Brownlee, R.A., Gorban, A.N., Levesley, J., Stability and stabilization of the lattice Boltzmann method, *Physical Review E*, 75, 2007, 1–17.
[25] Sfarra, S., Ibarra-Castanedo, C., Lambiase, F., Paoletti, D., Di Ilio, A., Maldague, X., From the experimental simulation to integrated non-destructive analysis by means of optical and infrared techniques: Results compared, *Measurement Science and Technology*, 23, 2012, 115601.
[26] Cao, Y., Dong, Y., Cao, Y., Yang, J., Yang, M.Y., Two-stream convolutional neural network for non-destructive subsurface defect detection via similarity comparison of lock-in thermography signals, *NDT and E International*, 112, 2020, 102246.
[27] McMasters, R.L., Brooke, G.M., David, J.A., Taylor, R.P., Chang, Y.H., LaRock, G., Valencia, K., Detecting material defects using a scanning laser beam, *Journal of Thermophysics and Heat Transfer*, 33, 2019, 210–215.
[28] The lattice Boltzmann method (continued), Computational Physics II, 2004.
[29] Mishra, S.C., Mondal, B., Kush, T., Krishna, B.S.R., Solving transient heat conduction problems on uniform and non-uniform lattices using the lattice Boltzmann method, *International Communications in Heat and Mass Transfer*, 36, 2009, 322–328.

ORCID iD

Brahim Addou https://orcid.org/0009-0000-6300-0786
Ben-Richou Abderrahim https://orcid.org/0009-0005-2288-9343
Balouki Abdessamad https://orcid.org/0000-0001-7806-8855
Azouz Jaouad https://orcid.org/0009-0002-0185-4334

How to cite this article: Addou B., et al., Numerical Study of Defects and Heat Transfer in Repaired Metallic Plates, *J. Appl. Comput. Mech.*, xx(x), 2026, 1–16. https://doi.org/10.22055/jacm.2026.48823.5532